



LAWRENCE  
LIVERMORE  
NATIONAL  
LABORATORY

# Residual stress and damage-induced critical fracture on CO<sub>2</sub> laser treated fused silica

M.J. Matthews, J.S. Stolken, R.M. Vignes, M.A. Norton, S. Yang, J.D. Cooke, G.M. Guss, J.J. Adams

November 10, 2009

Boulder Damage Symposium  
boulder, CO, United States  
September 21, 2009 through September 23, 2009

## **Disclaimer**

---

This document was prepared as an account of work sponsored by an agency of the United States government. Neither the United States government nor Lawrence Livermore National Security, LLC, nor any of their employees makes any warranty, expressed or implied, or assumes any legal liability or responsibility for the accuracy, completeness, or usefulness of any information, apparatus, product, or process disclosed, or represents that its use would not infringe privately owned rights. Reference herein to any specific commercial product, process, or service by trade name, trademark, manufacturer, or otherwise does not necessarily constitute or imply its endorsement, recommendation, or favoring by the United States government or Lawrence Livermore National Security, LLC. The views and opinions of authors expressed herein do not necessarily state or reflect those of the United States government or Lawrence Livermore National Security, LLC, and shall not be used for advertising or product endorsement purposes.

# **Residual stress and damage-induced critical fracture on CO<sub>2</sub> laser treated fused silica**

M.J. Matthews, J.S. Stolken, R.M. Vignes, M.A. Norton, S. Yang, J.D. Cooke, G.M. Guss, J.J. Adams

Lawrence Livermore National Laboratory, 7000 East Avenue, L-592, Livermore, CA 94550-9234 USA

## **ABSTRACT**

Localized damage repair and polishing of silica-based optics using mid- and far-IR CO<sub>2</sub> lasers has been shown to be an effective method for increasing optical damage threshold in the UV. However, it is known that CO<sub>2</sub> laser heating of silicate surfaces can lead to a level of residual stress capable of causing critical fracture either during or after laser treatment. Sufficient control of the surface temperature as a function of time and position is therefore required to limit this residual stress to an acceptable level to avoid critical fracture. In this work we present the results of 351 nm, 3ns Gaussian damage growth experiments within regions of varying residual stress caused by prior CO<sub>2</sub> laser exposures. Thermally stressed regions were non-destructively characterized using polarimetry and confocal Raman microscopy to measure the stress induced birefringence and fictive temperature respectively. For 1~40s square pulse CO<sub>2</sub> laser exposures created over 0.5-1.25kW/cm<sup>2</sup> with a 1-3mm 1/e<sup>2</sup> diameter beam ( $T_{\max} \sim 1500-3000\text{K}$ ), the critical damage site size leading to fracture increases weakly with peak temperature, but shows a stronger dependence on cooling rate, as predicted by finite element hydrodynamics simulations. Confocal micro-Raman was used to probe structural changes to the glass over different thermal histories and indicated a maximum fictive temperature of 1900K for  $T_{\max} \geq 2000\text{K}$ . The effect of cooling rate on fictive temperature caused by CO<sub>2</sub> laser heating are consistent with finite element calculations based on a Tool-Narayanaswamy relaxation model.

*Keyword list: residual stress, fracture, laser damage, finite element analysis*

# 1. INTRODUCTION

Surface heating using CO<sub>2</sub> lasers has proven effective at removing or reflowing damage on UV optics suitable in high power laser systems. For example, damage mitigation[1-2], surface polishing[3], cutting and surface patterning[4] using CO<sub>2</sub> lasers have been demonstrated and applied to silica-based materials with great success. These treatments generally require depositing enough laser energy to heat the glass above the transition/annealing point  $T_g$  and, in the case of ablation, up to and beyond the boiling point  $T_b$ . Figure 1 shows the viscosity[5] and vapor pressure[6] of silica as a function of temperature, indicating the range between  $T_g$  and  $T_b$ . It is well known however, that the brittle nature of glasses can make them prone to failure from thermal strains induced from non-uniform temperature fields. Silica, because of its relatively low thermal expansion coefficient ( $\sim 0.55\text{ppm/K}$ ) is less sensitive to thermal gradients during heating, but upon rapid cooling can accumulate a significant amount of *residual* stress due to the finite relaxation times near the glass transition. While not a known danger in and of itself with regard to damage initiation in high power lasers, upon introduction of a surface flaw/damage larger than some critical size, an extended fracture can occur to relieve stress throughout the heat-treated region. This critical fracture effect can cause an acceleration of damage growth such that the resulting diameter can quickly go beyond a treatable range in terms of subsequent damage mitigation. Furthermore, reflections from fracture boundaries near the surface can cause additional local damage initiations that also add to the effective damage growth. The relationship between maximum flaw length,  $a$ , and uniform critical stress  $\sigma_c$  at the critical fracture limit is given by[7]

$$\sigma_c = \frac{K_I}{\sqrt{\pi a}} \quad (1)$$

where  $K_I = 0.75 \text{ MPa}\cdot\text{m}^{-1/2}$  is the fracture toughness of fused silica. Because damage mitigation strategies generally specify a maximum treatable diameter, Eq. (1) describes the corresponding maximum allowable stress in a CO<sub>2</sub> treated zone. For example, a flaw/damage site around  $500\mu\text{m}$  in diameter would cause a critical fracture on silica surfaces with more than 20MPa of (tensile) stress. Therefore, CO<sub>2</sub> laser parameters that can achieve workable temperatures above  $T_g$ , while limiting the residual stress are crucial in preventing fractures upon incidental damage initiations.

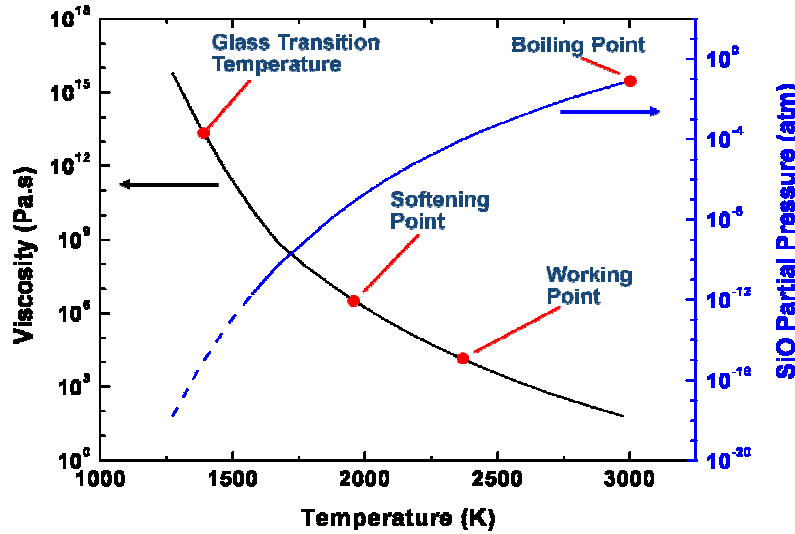


Figure 1: Viscosity and SiO partial pressure of SiO<sub>2</sub> as a function of temperature.

In this work, a CO<sub>2</sub> laser was used to heat fused silica surfaces to peak temperatures in the range 1600-3200K, over 1-100s of exposure time, and with various cooling sequences. Flaws are then introduced in the form of pulsed UV laser damage initiations and grown with subsequent UV pulses until the fracture limit is achieved and  $\sigma_c$  can be estimated. Finite element calculations are performed to explain the details of residual stress build up upon cooling, and the distribution of hoop and radial stresses throughout the heat affected zone. It will be shown that the critical stress correlates well with a maximum stress located not along the surface but 200-300 $\mu\text{m}$  below the surface for the

cases studied here. Finally, confocal Raman microscopy was performed to measure the fictive temperature and characterize the temperature-induced changes in the glass structure which lead to the final residual stress state. The measured fictive temperature depth profiles agree well with those calculated using a Tool-Narayanaswamy relaxation model and thermal histories predicted from finite element analysis. The possibility of using thermal only fictive temperature calculations to predict thermal stresses will be discussed.

## 2. EXPERIMENTAL

All samples were as-received, polished UV-grade Corning 7980 fused silica, 10mm thick by 51mm diameter round windows. A 10.6  $\mu\text{m}$  laser (Synrad firestar V20), with a maximum output power of 20 watts and power stability of  $\pm 5\%$ , is used for heating the fused silica sample. Beam power, diameter and  $\text{SiO}_2$  surface temperature are all monitored in real time. Heat-treated regions were created on the silica samples with varying maximum temperatures and cooling regimes. In all cases the temperature was either quenched by turning off the laser at the end of the heating time, or cooled (lower T hold, ramp) over a period equal to the heating time. The beam shape was nominally Gaussian with an asymmetry between long and short  $1/e^2$  diameters of less than 10%. Details of both the laser heating apparatus and in situ thermal measurements are described in more detail elsewhere[8]. Following 10.6  $\mu\text{m}$  laser exposures, each site was first imaged using cross-polarizers to identify the birefringence isoclines and then aligned to a frequency tripled Nd-YAG laser focal spot with a  $\sim 70\mu\text{m}$   $1/e^2$  diameter. Single 355nm, 10ns,  $\sim 60\text{J}/\text{cm}^2$  pulses were used to initiate a damage site of less than  $100\mu\text{m}$  diameter near the center of each stressed region. A large aperture ( $\sim 30\text{mm}$ ), 355nm laser at the optical sciences laboratory[9] was used to grow the damage sites with 5ns flat-in-time  $\sim 10\text{J}/\text{cm}^2$  pulses. After each pulse, the sample was taken out and the sites imaged (following a 30min wait) using a 5x microscope to inspect damage morphology. Laser shots continued until each site grew to a longest length (Feret's) diameter of  $>500\mu\text{m}$ .

A separate set of witness samples were created for Raman microscopy. Confocal Raman microscopy was carried out using a diode pumped frequency doubled Nd-YVO<sub>4</sub> laser operating at 532nm and in a back-scattering geometry with a 100x/0.70NA objective. A  $50\mu\text{m}$  core multimode fiber was used as the collection pinhole resulting in a confocal volume of approximately  $\pi 1^2 \times 5\mu\text{m}^3$ . Filtered Raman light was dispersed in an f/4 spectrophotometer with a 1200gr/mm grating and LN-cooled 1100x300 pixel CCD.

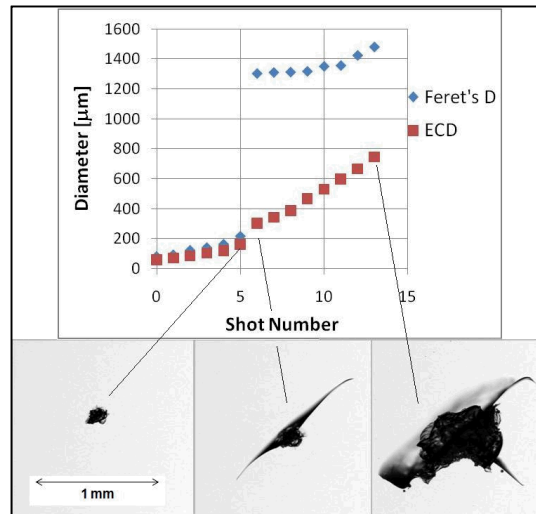


Figure 2: Diameter vs shot number for damage initiated in region treated by a  $\sim 60\text{s}$  10.6 $\mu\text{m}$  laser exposure with peak temperature  $\sim 2300\text{K}$ . The red dots are the measured effective circular diameter (ECD) which tracked mostly with the inner core area, while the blue dots are the longest length diameter (Feret's) which grew dramatically when the core reached a diameter of 200-300 $\mu\text{m}$ .

### 3. DAMAGE GROWTH AND CRITICAL FRACTURE

Figure 2 shows a typical sequence of damage growth shots and resulting morphologies of damage initiated within stressed regions. The particular site shown was exposed to a peak temperature of 2300K and quench-cooled. As shown, following the 7<sup>th</sup> shot, the residual stress within the region caused a dramatic radial fracture, quadrupling the Feret's diameter in the process. Afterwards, the ECD of the

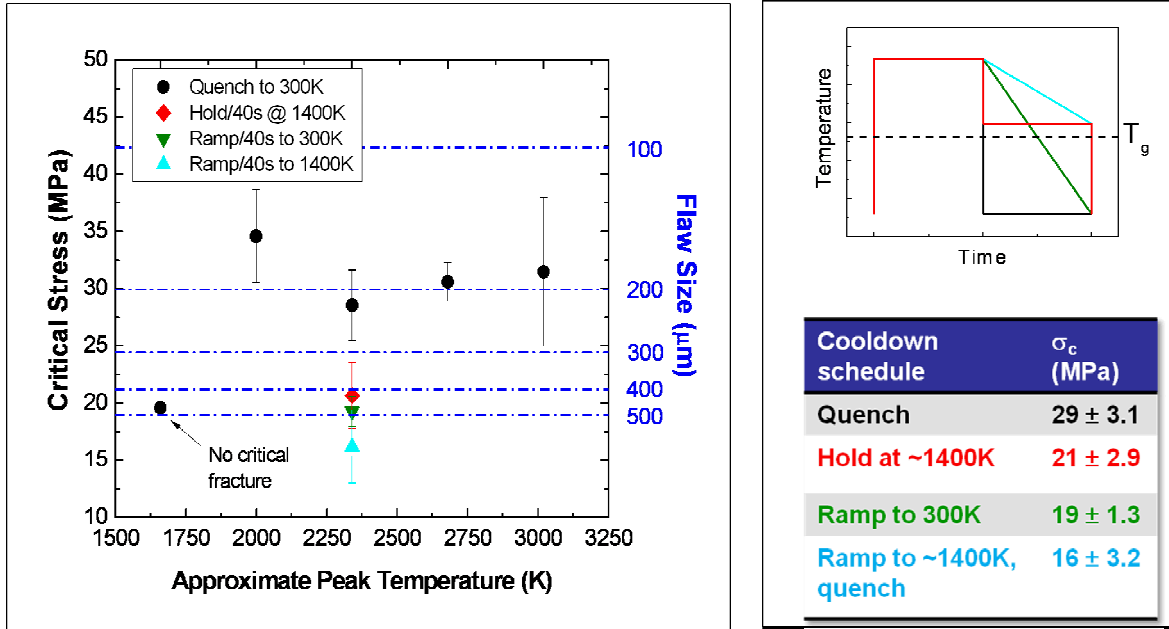


Figure 3: Flaw size, taken as the ECD just before fracture, and estimated critical stress using Eq. 1, plotted against peak temperature for various exposures and cooling cycles.

site grew at a rate roughly equal to that before the fracture event, while the Feret's diameter grew much more slowly. It is interesting to note that the ECD growth behavior was quite close to that predicted from previous unstressed experiments[10], namely  $ECD_{final} \sim ECD_{initial} \cdot \exp(\xi N)$  where  $\xi = 0.04 \cdot (\text{fluence} - 4.5)$  with fluence in  $J/cm^2$ , indicating that the residual stress apparently does not affect core growth rate. The ECD generally showed this exponential behavior throughout the growth shots, whereas the Feret's diameter approached a peak value. The morphology at the crack extremes indicated in the rightmost micrograph of Fig. 2 shows a curving of the crack tip in a tangential direction between shots 6 and 13. This curving behavior had the effect of limiting the extent of the overall damage.

The effect of increasing laser power and surface temperature on critical fracture behavior is shown in Fig. 3. In all cases, 2-4 radial cracks emanated from the site center, with the number of cracks scaling roughly with the measured peak temperature and appearing symmetrically distributed around the site. For surface temperatures below ~1700K, stress effects caused by quench seemed negligible up to damage site diameters of  $ECD \sim 500 \mu m$ . Between 2000 and 3000K, the effect of increasing peak temperature (or laser power) on allowable flaw size was weak, yielding critical stress values in the range 25~35MPa. A stronger dependence was observed between cooling methods. For a 2300K quench plus 'isothermal' hold with the on axis peak temperature just above the glass transition temperature, the estimated critical stress was roughly 8MPa lower than the quenched case, while the ramp downs showed a 10-13MPa decrease. In fact, virtually all cooling types for a peak 2300K treatment lowered critical stress and increased allowable flaw size to values close to the upper limit values of the 1700K case. However, it is significant that the 'hold' had the smallest effect, as will be discussed later. These results show the importance of avoiding rapid cool downs when attempting to minimize residual stress.

#### 4. FINITE ELEMENT ANALYSIS

Solving for the residual stress and plastic deformation of amorphous silica due to the deposition of energy by a laser requires a solution to a coupled system of partial differential equations: the heat equation, given by (2), and the balance of linear momentum, shown in (3).

$$\rho C_p \frac{\partial T}{\partial t} - \nabla \cdot (\kappa \nabla T) = Q \quad (2)$$

$$\text{div}(\boldsymbol{\sigma}) + \mathbf{b} = \rho \ddot{\mathbf{u}} \quad (3)$$

In (2) and (3),  $\rho$ ,  $C_p$  and  $\kappa$  are the density, specific heat capacity under constant pressure and the thermal conductivity respectively[11];  $T$  is the temperature field,  $t$  is time, and  $Q$  is an external energy source (in this case deposited by the laser),  $\boldsymbol{\sigma}$  is the Cauchy stress tensor,  $\mathbf{b}$  is the body force and  $\mathbf{u}$  is displacement with the raised double dots denoting two derivatives with respect to time. As this is a coupled thermal-mechanics problem, the divergence and gradient operators in (2) must be taken with respect to the current coordinate frame. The divergence operator in (3) is already in the current frame, as it has been written in lowercase lettering. Solving the above coupled equations is performed using a staggered, operator-split method[12] and applying only evaporative cooling[6] and traction-free surface boundary conditions for (2) and (3) respectively.

The heat source  $Q$  appearing in (2) caused by an absorbing incident Gaussian laser beam can be expressed as

$$Q(r, z, t) = \frac{\alpha P(t)}{\pi r_0^2} \exp(-\alpha z) \exp\left(-\frac{2r^2}{r_0^2}\right) \quad (4)$$

where  $\alpha$  is the absorption coefficient[13],  $P$  is the absorbed laser power, and  $r_0$  is the  $1/e^2$  radius of the laser beam. Finally, the constitutive equation describing the viscoelastic behavior of a glass can be written in terms of the usual Maxwell model as

$$\dot{\boldsymbol{\varepsilon}}' = \frac{\boldsymbol{\sigma}'}{\eta_o \cdot e^{\frac{\Delta H}{RT(t)}}} + \frac{\dot{\boldsymbol{\sigma}}'}{2 \cdot G} \quad (5)$$

The strain  $\boldsymbol{\varepsilon}$  in (5) responds elastically to stress through the shear modulus  $G$  in the second term, while a time dependent viscous response is described by the first term through an Arrhenius viscosity  $\eta = \eta_o \exp[\Delta H/RT(t)]$  where  $\Delta H$  is the activation energy[5]. Although not expressed explicitly, it should be recognized that in (2)-(5) the temperature dependence of the material properties  $\rho$ ,  $C_p$ ,  $\kappa$ ,  $\alpha$  must be taken into account to derive accurate thermal and mechanical predictions.

In creating an axisymmetric computational model for the finite element simulations, the smallest absorption depth of any  $\text{CO}_2$  laser used in the experiments was considered to ensure adequate mesh refinement. To sufficiently resolve the energy deposition, several elements had to be placed within an absorption depth of the surface; a  $10.6\mu\text{m}$  wavelength  $\text{CO}_2$  laser has the smallest absorption depth,  $4.0\mu\text{m}$  at  $2073.15\text{K}$ . To resolve the energy deposition, at least two elements were needed through the thickness of this absorption region, requiring a mesh spatial discretization of around  $2\mu\text{m}$ . As the computational simulations required an implicit time integration scheme to reach the experimental time periods on the order of seconds to minutes, it was desirable to limit the total number of elements. Instead of uniformly meshing the silica sample, a highly non-uniform meshing scheme was applied which resulted in a  $2\mu\text{m}$  by  $2\mu\text{m}$  meshing directly below the laser and gradually increased to the bottom outside edge of the sample. For the aforementioned cylindrical geometry of  $10 \times 51\text{mm}$  this yielded a mesh with 22,000 elements instead of the 62,500,000 elements which would have been required with a uniform mesh.

#### 5. COMPARISON OF SIMULATED STRESS FIELDS WITH FRACTURE EXPERIMENTS

We now consider the predicted stress fields caused by  $\text{CO}_2$  laser heating as the material heats up to a peak temperature of  $\sim 2000\text{K}$ . Far below the glass transition temperature, but above ambient temperature, thermal

expansion of the heated material causes a compressive strain to develop which falls off as  $\sim r^{-3/2}$  far from the beam center. At the incident surface, a net displacement of material creates a bump on the order of several hundred nanometers which is only weakly dependent on beam size and scales roughly at 100nm per watt of incident power. Compressive stresses build up until the maximum peak temperature exceeds  $T_g$  at which point the compressive stress is completely relaxed throughout the region  $T < T_g$ , and surrounding compressive stress decreases. As a result of this stress relaxation, the radial compressive stress is converted into an axial strain in the relaxed region, pushing material above the thermoelastically displaced surface boundary. Note that since  $T_g - T_0 \approx 1000K$ , the surface melt zone approximately ranges from  $0.69r_0$  to  $r_0$  for on-axis peak temperatures between the softening ( $\sim 1900K$ ) and boiling point ( $\sim 3000$ ) of fused silica. Figure 4a shows the hoop stress distribution at  $t=6.57s$  during a 10s exposure for  $r_0=500\mu m$  and  $P=5W$ . The resulting maximum temperature was 2007K and the melt zone is observed to extend to 350-400 $\mu m$  or  $0.7r_0$  to  $0.8r_0$  from beam center, in reasonable agreement with our analytical approximation ( $0.72r_0$ ).

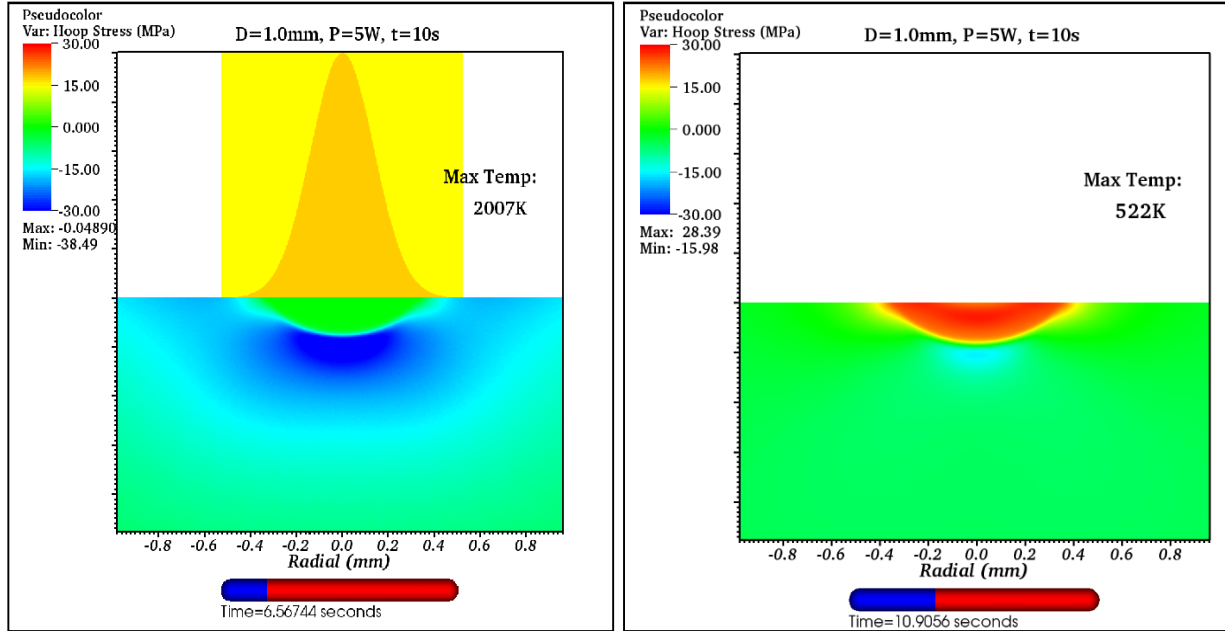


Figure 4: Cross section of hoop stress distribution within CO<sub>2</sub> laser heated fused silica at (a)  $t=6.57s$  and (b)  $t=10.9s$  for a 10s exposure of  $r_0=500\mu m$ ,  $P=5W$ . Tension is shown as positive/red while compression is shown as blue/negative.

This melt zone persists in a zero stress state until the laser is shut off and a rapid thermal quench ensues. Because the glass cannot completely relax the axially strained material over times short compared to stress relaxation times  $\tau=\eta/G$ , the surface above the formerly zero stress region is plastically deformed. Thus, as the surrounding material cools and contracts, what was the central melt zone has a slightly smaller subsurface volume and undergoes tensile strain as the body collectively cools. The resulting stress field 0.9 seconds after laser shut off is shown in Fig4b, where the zero stress zone is effectively replaced by a region with high tensile stress, with a small region in slight compression just below the region in tension. As observed by Bennett et al[14] for CO<sub>2</sub> laser treated borosilicate, the magnitude of the final residual tensile stress is nearly equal to the maximum compressive stress prior to cool down (20-30MPa).

It is interesting to note that the maximum normal stresses do not occur at  $z=r=0$ , but in fact reside in regions below the surface at  $r=0$  and off-axis for  $z=0$ . Figure 5 shows a plot of maximum hoop and radial tensile stress versus radial position, taken anywhere along the  $z$  direction, for a site heated to  $T_{max}\approx 2300K$  and quenched (critical fracture size  $\approx 200\mu m$ ). Also plotted is the axial position of the maximum hoop stress, which was nearly the same as that of the maximum radial stress. A micrograph of the damage site grown in a region heated with the laser conditions shown in Fig. 4 is overlaid on the graph, showing the correlation of the fracture morphology and the stress distribution around the site. At a depth of  $\sim 270\mu m$ , the peak hoop (and, by symmetry, radial) tensile stress was approximately 30MPa while at  $z=r=0$  the stress fell to 20MPa. The radial fractures clearly correspond to the hoop



stresses residing in the first 300 $\mu\text{m}$  of the surface, and in fact appeared deeper closer to the center, in general agreement with the stress distribution shown. Indeed, optical coherence tomography (not shown) also indicated that the crack depth decreased along the radial length of the fracture. Near the termination of the crack tip, the interesting curving behavior noted in the previous section can now be understood in terms of radial and hoop stress maxima: While the hoop (tensile) stress maxima monotonically decreases as a function of radius until turning compressive, the radial stress has a local maximum near the edge of the melt zone causing the crack propagation to go from radial to tangential. The relative increase in radial over hoop tensile stress therefore has the effect of limiting the extent of the fracture zone, and explains the slower overall growth of the Feret's diameter previously discussed.

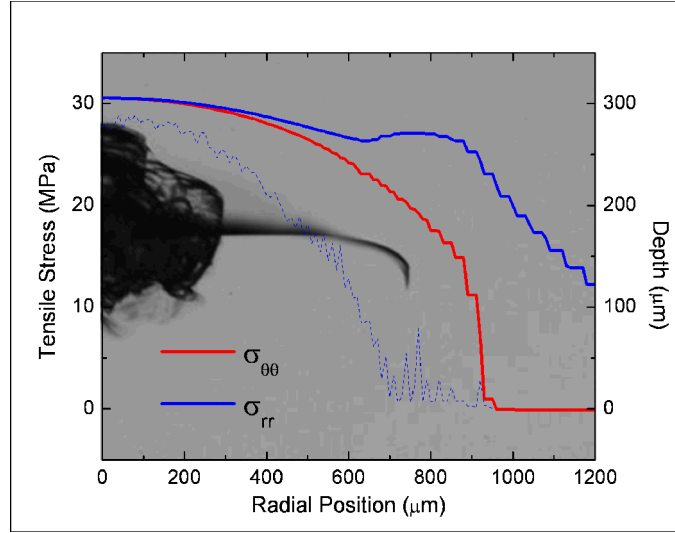


Figure 5: Left axis - Maximum radial (blue, solid) and hoop (red) tensile stress versus radial position taken anywhere in the axial direction as compared to the fracture morphology observed for the  $T_{\text{max}} \approx 2300\text{K}$  quench case. Right axis – Axial position of the maximum hoop stress

The effect of maximum temperature and cooling cycle is summarized in Table I. The second and third columns indicate the maximum temperature just before laser shut off and the maximum hoop stress, respectively. The last column is the estimated critical stress using eq. (1) and the observed damage site diameter coinciding with the critical fracture. As observed in the fracture experiments, the calculated maximum hoop stress only weakly increased with temperature ranging from 26.7 to 30.6 MPa for peak temperatures of 1700 – 2300K. A wider range of critical stress values were estimated from experiment, which is likely due to the non-uniformity in the damage morphology and the fact that the damage site itself is producing a stress field which may interact with that produced from the  $\text{CO}_2$  laser heating. Nonetheless, the calculated value for the maximum hoop stresses (26~31MPa) would predict critical failure for flaws roughly 200-350 $\mu\text{m}$  in size, which is remarkably close to the observed fracture behavior.

Table I: Summary of temperature and cooling dependence on calculated and estimated hoop stress.

	$T_{\text{max}}$ (K)	$\sigma_{\text{FEA}, \text{max}}$ (MPa)	$\sigma_c$ (MPa)
Quench	1700	26.7	$< 18.7 \pm 0.5$
Quench	2000	29.2	$34.5 \pm 4.0$
Quench	2300	30.6	$29 \pm 3.1$
Hold at 1400K	2300	29.0	$21 \pm 2.9$
Ramp to 1400K	2300	26.2	$16 \pm 3.2$
Ramp to 300K	2300	26.8	$19 \pm 1.3$

In the case of varying cool downs, the trend in the data followed that predicted, although the error bar overlap in the data precludes a definitive correlation. It is interesting to note that, unlike the isothermal hold recommended for

stress annealing in glass slabs, the hold near  $T_{\max} \sim T_g$  produced stress levels similar to that of the quench case. Only linear ramps appeared to produce a non-negligible amount of stress reduction, with the ramp to  $\sim T_g$  being slightly superior.

## 6. FICTIVE TEMPERATURE MEASUREMENTS

The complex stress distributions calculated in the preceding section clearly warrant a more precise experimental probe into viscoplasticity of heat affected regions. While polarimetry has been used to calibrate our model, and in general enjoys wide use as a measurement of stress-induced birefringence, as usually applied it only yields an integrated principal stress difference and does not indicate directly the individual stress components. Tomographic methods can be applied to deconvolve the stress tensor partially or completely, but are often difficult to implement.

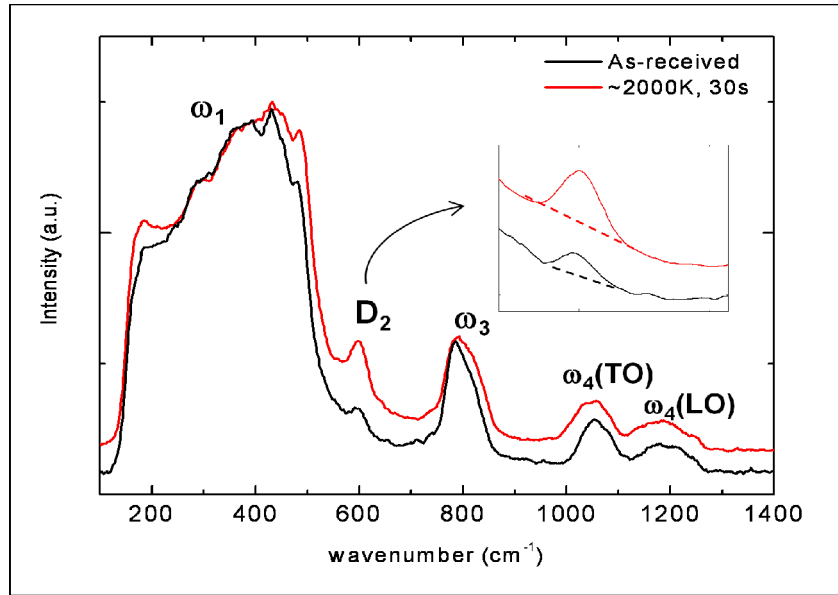


Figure 6: Typical Raman spectra measured for as received ( $T_f \sim 1315K$ ) and laser heated ( $T_f \sim 1900K$ ) fused silica indicated the change in  $D_2$  band intensity used to measure  $T_f$ .

Measurement of glass fictive temperature using vibrational spectroscopy has been used to study a wide range of glass-forming systems [15-16]. The fictive temperature,  $T_f$ , is defined as the temperature of the equilibrium melt whose structure is equivalent to that of the cooled glass. Although a single order parameter has been shown insufficient for completely describing silicate systems [17], characterization of  $T_f$  does yield meaningful insight to the thermal history. Most importantly for the question about stress, the fictive temperature is known to scale well with volumetric changes [18] so that measurement of  $T_f$  can be equated with measurement of strain from thermoplastic deformations.

Figure 6 shows two typical confocal micro-Raman spectra corresponding to as-received  $SiO_2$  and a region that was  $CO_2$  laser heated to  $\sim 2000K$ . Geissberger and Galeener [15] first studied the changes in the  $SiO_2$  Raman spectra for samples of different fictive temperature and showed that virtually all Raman bands shifted  $1-20\text{ cm}^{-1}$  for  $900 < T_f < 1700C$ . More dramatically, the intensities of the so-called ‘defect’ bands  $D_1$  and  $D_2$  were observed to increase with  $T_f$ , indicating a higher concentration of 4- and 3-ring Si-O groups at higher temperatures as predicted by quantum molecular dynamics [19]. Therefore, because of the higher sensitivity of the ring defect population with fictive temperature, we chose to measure the  $D_2$  band intensity, normalized to the  $\omega_1$  band at  $\sim 440\text{ cm}^{-1}$ , which can be related to  $T_f$  as

$$T_f = -\frac{E_a}{k_B \ln(I_{D_2} / I_0)} \quad (6)$$

Where  $E_a = 0.4 \pm 0.03$  eV is the  $D_2$  activation energy [15],  $k_B$  is Boltzmann's constant, and  $I_{D_2}$  is the normalized intensity of the  $D_2$  band.  $I_0$  is a calibration factor chosen such that  $T_f = T_g = 1315$ K on an as-received sample which was annealed in an  $N_2$  purged oven at  $T_g$  for 2.5 hours and ramped down at 5K/min. This calibration was further verified against  $T_f$  estimated from shifts in the Si-O-Si asymmetric stretch TO mode at  $\sim 1065$   $\text{cm}^{-1}$ , showing consistent behavior over the range of  $T_f$  studied here (1315-1900K).

A set of sites were measured over the same thermal history range as presented in the fracture studies, but absent of any damage initiation and growth. Spatially resolved axial scans were done along  $r=0$  to investigate the depth of the heat-affected zone and the relative changes to  $T_f$  over the first few hundred microns of the sample. The effect of varying peak temperature and cooling rate on  $T_f(z)$  is shown in Fig. 7. All quench and ramp cases studied displayed a characteristic sigmoidal shape with  $dT_f/dz \sim 0$  at the surface, and a mostly monotonic decrease into the bulk to  $T_f \sim T_g$ . Similar to the fracture experiments, the most dramatic change occurred from 1700 to 2000K and between quenched and non-quenched cases. For  $T_{\max} > 2000$ K,  $T_f$  at the surface was  $\sim 1900$ K, and the increase in peak temperature (laser power) only affected the maximum depth of the material with  $T_f > T_g$ . Since changes in  $T_f$  can be mapped to changes in local volume and hence strain gradients, these results seem to bolster the notion that there is a threshold behavior in the residual stress state created by quenched thermal treatments.

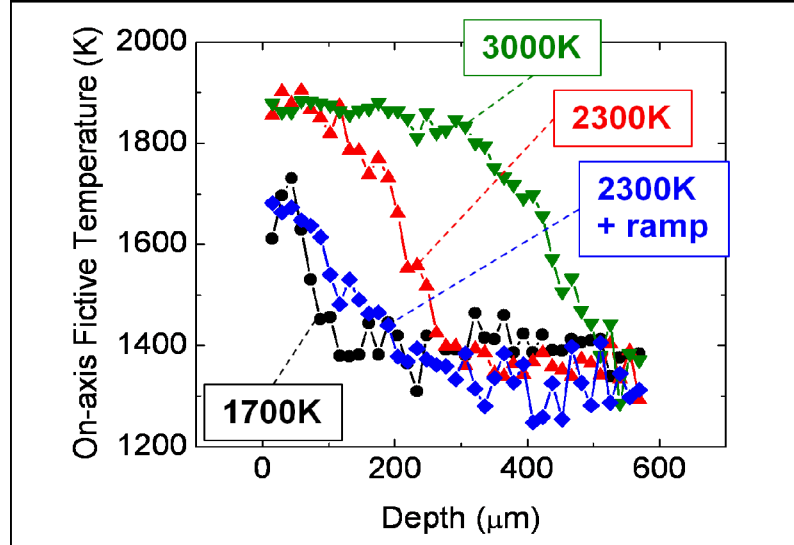


Figure 7: Depth profiles of the fictive temperature for thermally quenched silica sites at 1700, 2300 and 3000K peak temperatures compared to that of a  $T_{\max} \sim 2300$ K linear ramp to 300K site.

The peak in hoop stress away from  $z=r=0$  can also be understood in terms of the  $T_f(z)$  profiles observed in the Raman measurements. If one considers that the strain created between  $\text{SiO}_2$  regions of high and low  $T_f$  is somewhat similar to that encountered at the boundary layer in a lattice mis-matched system, the maximum stress should reside where the gradient in lattice constants is largest. Theoretically, the fictive temperature depends only on the thermal history and a relaxation function  $M(T, T_f, \tau)$  specific to the glass system in question[20]. As pointed out earlier, the dynamics of structural relaxation near  $T_g$ , and hence the exact form of  $M(T, T_f, \tau)$ , is a subject of continued debate and refinement[21], but behaves generally as  $M \rightarrow 0$  for  $T \gg T_g$  and  $M \rightarrow 1$  for  $T \sim T_g$ . Using the formalism of Markovskiy and Soules [20] and referencing the annealing point in the viscosity curve from Corning[22] such that  $\tau = \eta(1315\text{K})/G_\infty = 127\text{s}$ , we can formulate  $M$ , integrate over differential thermal history and compute  $T_f$  for comparison with the micro-Raman measurements. For the highest temperature quench cases shown in Fig. 7,  $T_{\max} = 2300$  and  $T_{\max} = 3000$ K, we compute a surface on-axis value of 1920K and 1940K respectively. Likewise, the lower temperature case and the 2300K ramp fictive temperatures were calculated to be 1600K and 1450K, respectively. The larger discrepancy for the ramp case is not presently understood. Nonetheless, the prospect of

evaluating the effect of thermal cycles on structural deformations and hence residual stress, could be useful as a development tool since thermal-only calculations require much less computing time compared to the full thermo-mechanical equivalent.

## 7. CONCLUSIONS

Sufficient control of the surface temperature during CO<sub>2</sub> laser heating of silica-based UV optics as a function of time and position is required to limit residual stress to an acceptable level and avoid critical fracture. 351 nm, 3ns Gaussian damage growth experiments within regions of varying residual stress caused by prior CO<sub>2</sub> laser exposures were studied to examine the behavior of critical fracture in these regions. While the core size of the damage increased with the number of UV laser pulses at a rate similar to previous studies of unstressed SiO<sub>2</sub>, the radial fracture associated with the residual stress grew more slowly after critical fracture and gradually moved tangentially. It was found that increasing peak temperature above 2000K only had a weak effect on the flaw size required to initiate critical fracture, while including a linear ramp cool down cycle or limiting  $T_{\max}$  to <2000K had a much stronger effect. Finite element analysis was used to model a coupled thermal-mechanical system which included a Maxwell viscoelastic relaxation term in the constitutive equation. The modeling results showed that the maximum in hoop and radial stress was located away from  $z=r=0$ , and that the spatial variation in  $\sigma_r$  versus  $\sigma_z$  could explain the tangential component and bounding behavior found in the critical fracture experiments. The critical stress estimated from fracture experiments using brittle fracture theory were in general agreement with maximum and surface hoop stresses predicted using finite element modeling and ranged from 16 – 35 MPa for the cases studied here. Thermally stressed regions were non-destructively characterized using polarimetry and confocal Raman microscopy to measure the stress induced birefringence and fictive temperature respectively. The  $T_f(z)$  profiles indicated that the effect of the lower temperature treatments or the non-quench cooling methods was to limit the magnitude but also the extent of material with high fictive temperature and thus decrease the total strain in the system.

## ACKNOWLEDGEMENTS

This work performed under the auspices of the U.S. Department of Energy by Lawrence Livermore National Laboratory under Contract DE-AC52-07NA27344

## REFERENCES

- [1] E. Mendez, K. M. Nowak, H. J. Baker, F. J. Villarreal, and D. R. Hall, "Localized CO<sub>2</sub> laser damage repair of fused silica optics," *Applied Optics*, vol. 45, pp. 5358-5367, Jul 2006.
- [2] I. L. Bass, V. G. Draggoo, G. M. Guss, R. P. Hackel, and M. A. Norton, "Mitigation of laser damage growth in fused silica NIF optics with a galvanometer scanned CO<sub>2</sub> laser - art. no. 62612A," in *Conference on High-Power Laser Ablation VI*, Taos, NM, 2006, pp. A2612-A2612.
- [3] K. M. Nowak, H. J. Baker, and D. R. Hall, "Efficient laser polishing of silica micro-optic components," *Applied Optics*, vol. 45, pp. 162-171, Jan 1 2006.
- [4] T. D. Bennett, D. J. Krajnovich, and L. Li, "Thermophysical modeling of bump formation during CO<sub>2</sub> laser texturing of silicate glasses," *Journal of Applied Physics*, vol. 85, pp. 153-159, Jan 1 1999.
- [5] R. H. Doremus, "Viscosity of silica," *Journal of Applied Physics*, vol. 92, pp. 7619-7629, Dec 2002.
- [6] H. L. Schick, "A thermodynamic analysis of the high-temperature vaporization properties of silica," *Chemical Reviews*, vol. 60, pp. 331-362, 1960.
- [7] B. Lawn, *Fracture of Brittle Solids - Second Edition*. New York: Cambridge University Press, 1993.
- [8] S. T. Yang, M. J. Matthews, and S. Elhadj, "Thermal transport in CO<sub>2</sub> laser irradiated fused silica: in situ measurements and analysis " *in press, Journal of Applied Physics*, 2009.

- [9] M. C. Nostrand, T. L. Weiland, R. L. Luthi, J. L. Vickers, W. D. Sell, J. A. Stanley, J. Honig, J. Auerbach, R. P. Hackel, and P. J. Wegner, "A large aperture, high energy laser system for optics and optical component testing," *Laser-Induced Damage in Optical Materials: 2003*, vol. 5273, pp. 325-333 540, 2003.
- [10] M. A. Norton, E. E. Donohue, M. D. Feit, R. P. Hackel, W. G. Hollingsworth, A. M. Rubenchik, and M. L. Spaeth, "Growth of laser damage in SiO<sub>2</sub> under multiple wavelength irradiation - art. no. 599108," in *37th Annual Boulder Damage Symposium on Optical Materials for High-Power Lasers*, Boulder, CO, 2005, pp. 99108-99108.
- [11] R. Bruckner, "Properties and Structure of Vitreous Silica I," *Journal of Non-crystalline Solids*, vol. 5, pp. 123-175, 1970.
- [12] F. Armero and J. C. Simo, "A new unconditionally stable fractional step method for nonlinear coupled thermomechanical problems," *International Journal for Numerical Methods in Engineering*, vol. 35, pp. 737-766, Sep 1992.
- [13] A. D. McLachlan and F. P. Meyer, "Temperature-dependence of the extinction coefficient of fused-silica for CO<sub>2</sub>-laser wavelengths," *Applied Optics*, vol. 26, pp. 1728-1731, May 1987.
- [14] T. D. Bennett and L. Li, "Modeling laser texturing of silicate glass," *Journal of Applied Physics*, vol. 89, pp. 942-950, Jan 15 2001.
- [15] A. E. Geissberger and F. L. Galeener, "Raman studies of vitreous SiO<sub>2</sub> versus fictive temperature," *Physical Review B*, vol. 28, pp. 3266-3271, 1983.
- [16] S. R. Ryu and M. Tomozawa, "Fictive temperature measurement of amorphous SiO<sub>2</sub> films by IR method," *Journal of Non-Crystalline Solids*, vol. 352, pp. 3929-3935, Oct 1 2006.
- [17] G. W. Scherer, "Theories of Relaxation," *Journal of Non-Crystalline Solids*, vol. 123, pp. 75-89, Aug 1990.
- [18] J. E. Shelby, "Density of vitreous silica," *Journal of Non-Crystalline Solids*, vol. 349, pp. 331-336, Dec 1 2004.
- [19] A. Pasquarello and R. Car, "Identification of Raman defect lines as signatures of ring structures in vitreous silica," *Physical Review Letters*, vol. 80, pp. 5145-5147, Jun 8 1998.
- [20] O. S. Narayanaswamy, "Stress and Structural Relaxation in Tempering Glass," *Journal of the American Ceramic Society*, vol. 61, pp. 146-152, 1978.
- [21] C. A. Angell, "Formation of Glasses from Liquids and Biopolymers," *Science*, vol. 267, pp. 1924-1935, Mar 31 1995.
- [22] Corning 7980 Datasheet. Available:  
[http://www.corning.com/docs/specialtymaterials/pisheets/H0607\\_hpfs\\_Standard\\_ProductSheet.pdf](http://www.corning.com/docs/specialtymaterials/pisheets/H0607_hpfs_Standard_ProductSheet.pdf)